Scaling of asymmetric magnetic reconnection: General theory and collisional simulations

P. A. Cassak and M. A. Shay
Department of Physics and Astronomy, University of Delaware, Newark, Delaware 19716, USA

(Received 10 July 2007; accepted 19 September 2007; published online 31 October 2007)

A Sweet-Parker-type scaling analysis for asymmetric antiparallel reconnection (in which the reconnecting magnetic field strengths and plasma densities are different on opposite sides of the dissipation region) is performed. Scaling laws for the reconnection rate, outflow speed, the density of the outflow, and the structure of the dissipation region are derived from first principles. These results are independent of the dissipation mechanism. It is shown that a generic feature of asymmetric reconnection is that the X-line and stagnation point are not colocated, leading to a bulk flow of plasma across the X-line. The scaling laws are verified using two-dimensional resistive magnetohydrodynamics numerical simulations for the special case of asymmetric magnetic fields with symmetric density. Observational signatures and applications to reconnection in the magnetosphere are discussed. © *2007 American Institute of Physics*. [DOI: 10.1063/1.2795630]

I. INTRODUCTION

Magnetic reconnection converts magnetic energy into particle and flow energy in many space, astrophysical, and laboratory applications. Examples include solar flares, magnetic substorms, and sawtooth crashes in fusion devices. Models of reconnection have evolved from the Sweet-Parker model[1,2] of collisional reconnection, which is far too slow to explain observed phenomena, to the Petschek model,[3] where slow shocks mediate fast reconnection, to collisionless (Hall) reconnection (see, for example, Refs. 4–6), which has enjoyed wide success in explaining laboratory and magnetospheric observations.

Reconnection described by these models is usually studied in simplified geometries and ambient conditions, namely in two dimensions with the plasmas on either side of the dissipation region having identical densities and magnetic field strengths. However, this canonical description is rarely realized in nature.

The most glaring example of an asymmetry across the dissipation region is at the dayside of the magnetopause, where the magnetosheath plasma (with a magnetic field of 20–30 nT and a density of 20–30 cm^{-3}) reconnects with the magnetospheric plasma (with a magnetic field of 50–60 nT and a density of 0.3–0.5 cm^{-3}).[7,8] Satellite observations of flux transfer events (FTEs),[9,10] short-lived reconnection events at the dayside magnetopause, reveal asymmetric signatures in a significant fraction of events.[11] Also, at the onset of geomagnetic storms, a cold and dense ($\sim$50 cm^{-3}) plasma from the plasmasphere convects toward the dayside, forming a "plasmaspheric drainage plume,"[12] which can affect reconnection at the dayside.[13] Asymmetric magnetic reconnection has also been observed in the distant magnetotail[14] where the densities can be different by a factor of 10 due to asymmetric mass loading from the dayside during periods of dawnward interplanetary magnetic field (IMF),[15] and in the solar wind[16] downstream of the Earth, where the Alfvén speed on opposite sides of the reconnection outflow can be different by up to a factor of 2. Other examples are in tokamak plasmas, where the density and magnetic field strength profiles change with major radius, making reconnection manifestly asymmetric, and in the solar corona when an emergent flux tube reconnects with overlying arcades.

The effect of asymmetric conditions (in particular at the magnetopause) on the Petschek model of reconnection was addressed soon after its introduction.[17] It was suggested that as one crosses the dissipation region, the slow shocks mediating symmetric reconnection become an intermediate wave at which the field changes directions followed by a slow expansion fan at which the gas pressure drops. Numerous studies since then have addressed the shock and wave structure of Petschek reconnection at the magnetopause using fluid,[8,18–25] hybrid,[21,26–31] and particle[32] numerical simulations and analytic theory.[33–37] Another relevant study is a hybrid simulation of flux rope and core field generation at the magnetopause.[38]

Surprisingly, despite the interest in the shock structure, few basic studies of the properties of the dissipation region have been performed. Swisdak *et al.*[39] studied the effect on the reconnection rate of a density gradient across the dissipation region during reconnection with an out-of-plane (guide) magnetic field using particle simulations. More recently, Borovsky and Hesse[40] numerically studied the scaling of reconnection with asymmetric densities using magnetohydrodynamic simulations with anomalous resistivity. Swisdak and Drake[41] presented a model for determining in which plane reconnection occurs between magnetic fields of arbitrary strength and orientation. However, a general theory of the structure of the dissipation region and the rate of reconnection during asymmetric reconnection does not currently exist.

This paper intends to fill that void by developing a theoretical framework for studies of asymmetric reconnection. We derive analytical expressions from first principles using a Sweet-Parker-type scaling analysis. For simplicity, we treat two-dimensional antiparallel magnetic reconnection. When applied to a collisional plasma, the results generalize the classical Sweet-Parker model to allow for asymmetric mag-

netic fields and densities. However, most of the scaling results are independent of the dissipation mechanism and, therefore, apply to collisionless and anomalous resistivity models of asymmetric reconnection as well.

Furthermore, we show that a generic feature of asymmetric reconnection is that the X-line and stagnation point are not colocated. This implies that there is a bulk flow of plasma through the X-line, as has been noted in previous numerical studies and is often observed at the dayside magnetopause. We provide the physical foundation for this effect.

General scaling laws for asymmetric reconnection are derived in Sec. II and verified with resistive magnetohydrodynamic numerical simulations in Sec. III. Observational signatures of asymmetric reconnection are discussed in Sec. IV. Conclusions and applications to magnetospheric observations are discussed in Sec. V. This paper does not address the shock structure of asymmetric reconnection.

II. DERIVATION OF SCALING LAWS

The standard Sweet-Parker scaling laws for collisional reconnection can be obtained using the laws of conservation of mass, conservation of energy, and conservation of magnetic flux. For asymmetric reconnection, care must be taken. To remain in a steady state, the magnetic flux entering the dissipation region from the two upstream edges of the dissipation region must be equal. If the upstream magnetic field strengths are different on either side of the dissipation region, the flux from the stronger field plasma must enter more slowly than the flux from the weaker field plasma. As such, it is the *flux* of mass and energy through the dissipation region that must be balanced to achieve a steady state.

Scaling laws for the outflow speed and the reconnection rate can be derived by balancing the flux of mass, energy, and magnetic flux into and out of the dissipation region. A formal derivation uses the equations of magnetohydrodynamics (MHD) in conservative form,

$$\frac{\partial \rho}{\partial t} = -\nabla \cdot (\rho \mathbf{v}), \tag{1}$$

$$\frac{\partial (\rho \mathbf{v})}{\partial t} = -\nabla \cdot \left[\rho \mathbf{v}\mathbf{v} + \left(P + \frac{B^2}{8\pi} \right) \mathbf{I} - \frac{\mathbf{B}\mathbf{B}}{4\pi} \right], \tag{2}$$

$$\frac{\partial \mathcal{E}}{\partial t} = -\nabla \cdot \left[\left(\mathcal{E} + P + \frac{B^2}{8\pi} \right) \mathbf{v} - \frac{(\mathbf{v} \cdot \mathbf{B})}{4\pi} \mathbf{B} \right], \tag{3}$$

$$\frac{\partial \mathbf{B}}{\partial t} = -c \nabla \times \mathbf{E}, \tag{4}$$

$$\mathbf{E} = -\frac{\mathbf{v} \times \mathbf{B}}{c} + \mathbf{R}, \tag{5}$$

where ρ is the plasma mass density, $\mathbf{v}$ is the flow velocity, P is the pressure, $\mathbf{B}$ is the magnetic field, $\mathbf{E}$ is the electric field, $\mathcal{E} = (1/2)\rho v^2 + P/(\gamma - 1) + B^2/8\pi$ is the total energy density, and $\mathbf{I}$ is the unit tensor. The ratio of specific heats is γ, and $\mathbf{R}$ contains all the other terms in the generalized Ohm's law.

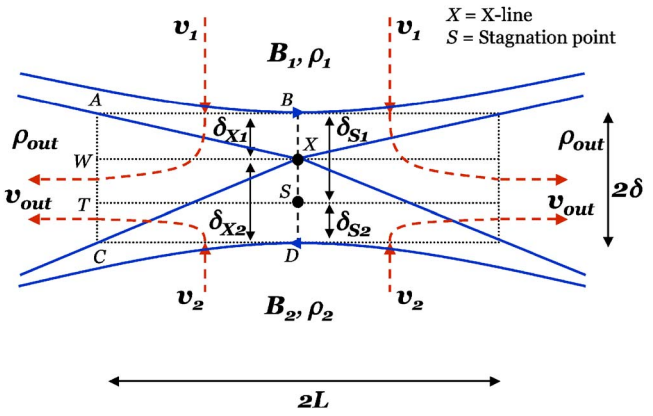

FIG. 1. (Color online) Schematic diagram of the dissipation region during asymmetric reconnection. Quantities above and below the dissipation region have a subscript of "1" and "2," respectively. Quantities describing the outflow have "out" subscripts. The magnetic field lines are the (blue) solid lines, the velocity flow is the (red) dashed lines. The points *X* and *S* mark the X-line and the stagnation point, which are not colocated. The edges of the dissipation region and lines through the X-line and stagnation point are marked by dotted lines.

Integrate the evolution equations over an arbitrary volume V. We consider reconnection in a steady state, for which all temporal derivatives vanish. Using Gauss' theorem, the evolution equations for mass, momentum, and energy give

$$\oint_S d\mathbf{S} \cdot (\rho \mathbf{v}) = 0, \tag{6}$$

$$\oint_S d\mathbf{S} \cdot \left[\rho \mathbf{v}\mathbf{v} + \left(P + \frac{B^2}{8\pi} \right) \mathbf{I} - \frac{\mathbf{B}\mathbf{B}}{4\pi} \right] = 0, \tag{7}$$

$$\oint_S d\mathbf{S} \cdot \left[\left(\mathcal{E} + P + \frac{B^2}{8\pi} \right) \mathbf{v} - \frac{(\mathbf{v} \cdot \mathbf{B})}{4\pi} \mathbf{B} \right] = 0, \tag{8}$$

where S is the surface of V and $d\mathbf{S}$ is the area element pointing in the outward normal direction. Using Stokes' theorem, Faraday's law gives

$$\oint_S d\mathbf{S} \times \mathbf{E} = 0. \tag{9}$$

These four equations are valid for any volume V, provided a steady state has been reached. Consider two-dimensional reconnection where there is no variation in the out-of-plane direction. Model the dissipation region as a box of half-width δ and half-length L, as depicted as the outer dotted line in Fig. 1. Let V extend an arbitrary height h out of the plane, with edges in the plane defined by the rectangle $ABCD$ in Fig. 1. The requirement of mass continuity [Eq. (6)] for this volume gives

$$L(\rho_1 v_1 + \rho_2 v_2) \sim 2\delta(\rho_{\text{out}} v_{\text{out}}), \tag{10}$$

where the "1", "2," and "out" subscripts refer to properties upstream and above, upstream and below, and in the outflow region, respectively. By symmetry, the mass flux through the midplane (BD) is zero. We use $\sim$ to mean "scales-like." A similar analysis of the momentum equation [Eq. (7)] only enforces pressure balance across and along the current sheet.

The energy equation [Eq. (8)] evaluated for the same volume, assuming the pressure does not play a major role in energy conversion for scaling purposes, gives

$$L\left(\frac{B_1^2}{8\pi}v_1+\frac{B_2^2}{8\pi}v_2\right)\sim 2\delta\left(\frac{1}{2}\rho_{\text{out}}v_{out}^2\right)v_{\text{out}}, \tag{11}$$

where B_1 and B_2 are the magnetic field strengths upstream above and upstream below the dissipation region. The dominant contribution to the energy density $\mathcal{E}$ is magnetic on the upstream edges (AB and CD), is kinetic on the downstream edge (AC), and vanishes at the midplane (BD). The term proportional to $\mathbf{v}\cdot\mathbf{B}$ in the energy flux equation is negligible because $\mathbf{B}\cdot d\mathbf{S}\simeq 0$. Evaluating the component of Faraday's law [Eq. (9)] in the outflow direction for the same volume gives

$$v_1B_1\sim v_2B_2, \tag{12}$$

where we use Eq. (5) and note that $\mathbf{R}$ vanishes at the edge of the dissipation region by definition.

Treating the upstream values of density and magnetic field strength as known or measurable, we immediately obtain an expression for the outflow speed v_{out}. Dividing Eq. (11) by Eq. (10) and eliminating v_2 using Eq. (12) yields

$$v_{\text{out}}^2\sim\frac{B_1B_2}{4\pi}\frac{B_1+B_2}{\rho_1B_2+\rho_2B_1}. \tag{13}$$

Note, this relation is invariant under a relabeling of 1 and 2, as it must be. This equation was rederived independently for a different application in Ref. 41, which we discuss in Sec. V. In the limit of symmetric fields and densities ($B_1=B_2\equiv B$ and $\rho_1=\rho_2\equiv\rho$), Eq. (13) reduces to the standard Sweet-Parker result of $v_{\text{out}}^2\sim B^2/4\pi\rho$. When the magnetic fields are symmetric ($B_1=B_2\equiv B$) but the densities are asymmetric, it reduces to

$$v_{\text{out}}^2\sim\frac{B^2}{4\pi(\rho_1+\rho_2)/2}, \tag{14}$$

the Alfvén speed based on the *arithmetic* mean of the densities. When the densities are symmetric ($\rho_1=\rho_2\equiv\rho$) but the magnetic fields are asymmetric, Eq. (13) reduces to

$$v_{\text{out}}^2\sim\frac{B_1B_2}{4\pi\rho}, \tag{15}$$

the Alfvén speed based on the *geometric* mean of the upstream magnetic fields.

Returning to Eq. (11), we find an expression for the reconnection rate $E\sim v_1B_1/c\sim v_2B_2/c$. Eliminating the inflow velocities and using Eq. (12) gives

$$E\sim\left(\frac{\rho_{\text{out}}B_1B_2}{\rho_1B_2+\rho_2B_1}\right)\frac{v_{\text{out}}}{c}\frac{2\delta}{L}, \tag{16}$$

where we used Eq. (13) to eliminate two factors of v_{out}.

The density ρ_{out} in the outflow region is difficult to calculate from first principles. We assume that ρ_{out} scales like the effective mass density of a newly reconnected flux tube, as was assumed for the symmetric magnetic field case in Ref. 40. Consider the reconnection of two flux tubes containing magnetic flux ψ. If the magnetic field strengths are different,

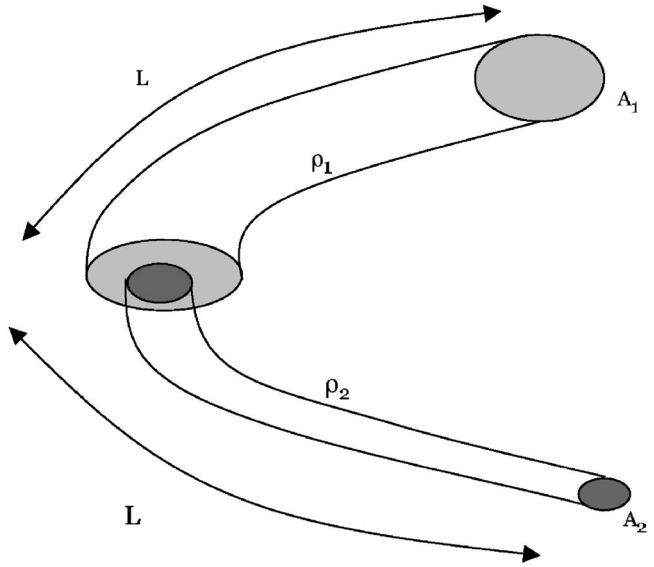

FIG. 2. A newly reconnected flux tube during asymmetric reconnection. The cross-sectional areas are A_1 and A_2 and the length is L.

the cross-sectional area A of the flux tubes is different (see Fig. 2). In particular, $\psi\sim B_1A_1\sim B_2A_2$. Then, the effective mass density is the total mass $\rho_1A_1L+\rho_2A_2L$ divided by the total volume A_1L+A_2L. Using $A_2\sim A_1B_1/B_2$, one finds

$$\rho_{\text{out}}\sim\frac{\rho_1B_2+\rho_2B_1}{B_1+B_2}. \tag{17}$$

When the upstream densities are symmetric, ρ_{out} is their common value independent of the fields, and when the fields are symmetric, ρ_{out} is the average of the upstream densities, as is to be expected. That ρ_{out} scales like the effective mass density of the newly reconnected flux tube assumes that the volume of the flux tube does not change while the mass in the flux tube redistributes itself. (This assumption is equivalent to assuming that the volume of plasma flowing into the dissipation region per unit time scales like the volume of plasma flowing out per unit time: $Lv_1+Lv_2\sim 2\delta v_{\text{out}}$.) Equation (17) may need to be modified for strongly asymmetric systems as the assumptions may not be tenable.

The expressions for the outflow speed and reconnection rate simplify using the expression for ρ_{out} in Eq. (17). In particular, eliminating ρ_{out} from Eq. (13) gives

$$v_{\text{out}}^2\sim\frac{B_1B_2}{4\pi\rho_{\text{out}}}. \tag{18}$$

That is, the general outflow speed scales like the Alfvén speed based on the geometric mean of the upstream fields and the density of the outflow. Eliminating ρ_{out} from Eq. (16) gives

$$E\sim\left(\frac{B_1B_2}{B_1+B_2}\right)\frac{v_{\text{out}}}{c}\frac{2\delta}{L}. \tag{19}$$

This expression reveals that the reconnection rate is a product of the aspect ratio of the dissipation region, the outflow speed, and an effective magnetic field strength given by the "reduced" field. We remind the reader that Eqs. (13) and (16)

are valid independent of the assumptions made about the outflow density.

It is important to note that the dissipation mechanism has not been specified, so the results thus far describe asymmetric reconnection in general.

We now turn to the structure of the dissipation region. In particular, where is the X-line located? Using Eq. (12), one sees that the strong magnetic field is convected into the dissipation region more slowly than the weak magnetic field. From this result, one might expect the X-line to be offset from the center of the dissipation region toward the strong field side. However, this is not the case. The crux is that while the velocity is greater on the weak field side, the flux of magnetic energy $\propto vB^2$ is smaller. Since there is no flux of magnetic energy across the X-line and the outflux of kinetic energy is relatively evenly distributed across the outflow edge of the dissipation region, the X-line is actually offset toward the *weak* field side.

Interestingly, the same line of reasoning applies to the location of the stagnation point of the flow within the dissipation region. The stagnation point is displaced from the center of the dissipation region to whichever side has the smaller mass flux into the dissipation region. Since the mass flux $\propto \rho v \propto \rho/B$, the stagnation point is displaced to whichever side has a smaller ρ/B. This can be either toward the strong or weak magnetic field side depending on the densities.

The immediate corollary to these two arguments is that, unlike in symmetric reconnection, the X-line and stagnation point need not be colocated and, in general, will not be. This implies that there is a net bulk flow of plasma across the X-line during asymmetric reconnection. This is intimately related to the result of Ref. 17, which stated that the waves available to change the field and density require two steps (an intermediate wave and a slow expansion fan).

Once again, the present arguments are independent of the dissipation mechanism. Therefore, the decoupling of the X-line and the stagnation point is a generic feature of asymmetric reconnection.

The interior structure of the dissipation region, in light of the present discussion, is sketched in Fig. 1. The dotted line through *WX* is the neutral line where the magnetic field goes through zero, with the X-line at its center (marked *X*). The distance from the top and bottom edges of the dissipation region to the X-line (*BX* and *DX*) is defined as δ_{X1} and δ_{X2}. The dotted line through *ST* is where the inflow velocity goes through zero, with the stagnation point at its center (marked *S*). The distance from the upstream edges to the stagnation point (*BS* and *DS*) is defined as δ_{S1} and δ_{S2}. These length scales satisfy the relationship

$$2\delta = \delta_{X1} + \delta_{X2} = \delta_{S1} + \delta_{S2}. \tag{20}$$

We define the distance between the X-line and the stagnation point as δ_{XS}. Therefore,

$$\delta_{XS} = \delta_{S1} - \delta_{X1} = \delta_{X2} - \delta_{S2}. \tag{21}$$

We now turn to deriving analytic expressions for the location of the X-line and stagnation point within the dissipation region. The analysis proceeds by returning to the conservation laws in Eqs. (6)–(9), which hold for arbitrary volumes. For the energy equation [Eq. (8)], we choose the volume extending from the top edge to the neutral line (labeled *ABXW* in Fig. 1). The key is that the magnetic energy through the neutral line *WX* is zero, the flow energy across it can be shown to be negligible, and there is no flux through the midplane *BX* by symmetry. Therefore, energy balance requires

$$L\left(\frac{B_1^2}{8\pi}v_1\right) \sim \delta_{X1}\left(\frac{1}{2}\rho_{\text{out}}v_{\text{out}}^2\right)v_{\text{out}}. \tag{22}$$

Similarly, using the lower volume *CDST* gives

$$L\left(\frac{B_2^2}{8\pi}v_2\right) \sim \delta_{X2}\left(\frac{1}{2}\rho_{\text{out}}v_{\text{out}}^2\right)v_{\text{out}}. \tag{23}$$

The sum of these two equations reproduces Eq. (11).

For the mass equation [Eq. (6)], we choose the volume extending from the top edge to the line through the stagnation point, labeled *ABST* in Fig. 1. Since the mass flux across the stagnation point *ST* and the midplane *BS* vanishes, mass conservation requires

$$L(\rho_1 v_1) \sim \delta_{S1}(\rho_{\text{out}}v_{\text{out}}). \tag{24}$$

Similarly, using the lower volume *CDST* gives

$$L(\rho_2 v_2) \sim \delta_{S2}(\rho_{\text{out}}v_{\text{out}}). \tag{25}$$

The sum of these two equations reproduces Eq. (10).

Taking the ratio of Eq. (23) to Eq. (22) and using Eq. (12) yields

$$\frac{\delta_{X2}}{\delta_{X1}} \sim \frac{B_2}{B_1}. \tag{26}$$

This quantifies the result that the X-line is offset toward the plasma with the weaker magnetic field. Similarly, the ratio of Eq. (25) to Eq. (24) gives

$$\frac{\delta_{S2}}{\delta_{S1}} \sim \frac{\rho_2 B_1}{\rho_1 B_2}, \tag{27}$$

which quantifies the result that the stagnation point is offset toward whichever side has the smaller value of ρ/B. We return to the relative location of the X-line and stagnation point in Sec. IV.

Other relationships between these length scales are obtained by taking the ratio of Eq. (22) to Eq. (24) and Eq. (23) to Eq. (25), giving

$$\frac{\delta_{X1}}{\delta_{S1}} \sim \frac{\rho_{\text{out}}B_1}{\rho_1 B_2} \quad \text{and} \quad \frac{\delta_{X2}}{\delta_{S2}} \sim \frac{\rho_{\text{out}}B_2}{\rho_2 B_1}, \tag{28}$$

where we used Eq. (18). Similarly, the ratio of Eq. (22) to Eq. (25) and Eq. (23) to Eq. (24) gives

$$\frac{\delta_{X1}}{\delta_{S2}} \sim \frac{\rho_{\text{out}}}{\rho_2} \quad \text{and} \quad \frac{\delta_{X2}}{\delta_{S1}} \sim \frac{\rho_{\text{out}}}{\rho_1}. \tag{29}$$

Also, using Eqs. (26) and (21), one can show

$$\frac{\delta_{XS}}{\delta_{X1}} \sim \frac{\rho_1 B_2 - \rho_{\text{out}} B_1}{\rho_{\text{out}} B_1}, \tag{30}$$

which relates the distance from the X-line to the stagnation point to the upstream densities and magnetic field strengths. Once again, we reiterate that the dissipation mechanism has not entered the present analysis, so Eqs. (22)–(30) hold for asymmetric fast reconnection in general. We also note that Eqs. (26) and (27) are valid independent of the assumptions used in estimating ρ_{out} in Eq. (17).

Just as in symmetric reconnection, in order to find the reconnection rate and absolute size of the dissipation region in terms of upstream quantities, a dissipation mechanism must finally be introduced. Since complete theories of collisionless or anomalous resistivity mediated reconnection do not even exist for symmetric reconnection, and for the purposes of making comparisons to numerical simulations, we consider asymmetric collisional reconnection, thereby extending the Sweet-Parker model to asymmetric systems. Thus, let $\mathbf{R}=\eta\mathbf{J}$ in Eq. (5), where η is a constant and uniform resistivity and $\mathbf{J}=(c/4\pi)\nabla\times\mathbf{B}$ is the current density.

Evaluating the outflow component of Eq. (9) over the domain *ABXW* going through the neutral line and using Eq. (5), one finds $v_1 B_1/c \sim \eta J_X$, where J_X is the out-of-plane current density at the X-line. Taking $J_X \sim cB_1/4\pi\delta_{X1}$, this gives

$$v_1 \sim \frac{\eta c^2}{4\pi\delta_{X1}}. \tag{31}$$

(By a similar argument, $v_2 \sim \eta c^2/4\pi\delta_{X2}$.) Beginning from Eq. (19) and using Eq. (20), one can eliminate δ_{X2} using Eq. (26), leaving

$$v_1 \sim \left(\frac{B_2}{B_1}\right) v_{\text{out}} \frac{\delta_{X1}}{L},$$

where we used $E \sim v_1 B_1/c$. Solving the previous two equations simultaneously gives

$$\delta_{X1} \sim \sqrt{\frac{\eta c^2 L}{4\pi v_{\text{out}}} \frac{B_1}{B_2}}. \tag{32}$$

Using Eq. (26),

$$\delta_{X2} \sim \sqrt{\frac{\eta c^2 L}{4\pi v_{\text{out}}} \frac{B_2}{B_1}}. \tag{33}$$

Using Eqs. (31), (32), and (12) gives

$$v_1 \sim \sqrt{\frac{\eta c^2 v_{\text{out}}}{4\pi L} \frac{B_2}{B_1}} \quad \text{and} \quad v_2 \sim \sqrt{\frac{\eta c^2 v_{\text{out}}}{4\pi L} \frac{B_1}{B_2}}. \tag{34}$$

Finally, the reconnection rate is, using $E \sim v_1 B_1/c$,

$$E \sim \frac{1}{c} \sqrt{\frac{\eta c^2 v_{\text{out}}}{4\pi L} B_1 B_2}. \tag{35}$$

Expressions (32)–(35), with v_{out} given by Eq. (13), specify the salient quantities, *specifically for asymmetric Sweet-Parker reconnection*, in terms of the magnetic fields and densities upstream of the dissipation region. The length of the dissipation region L for Sweet-Parker reconnection extends to length scales of the order of the system size,[42–44] and is taken as a known quantity. Note, the expression for the reconnection rate is invariant under an interchange of "1" and "2," as it must be. Further, these results reduce to the standard Sweet-Parker results in the symmetric limit, as they must.

III. NUMERICAL SIMULATION RESULTS

The scaling results from the preceding section are verified in the limit of asymmetric magnetic fields with symmetric densities in a collisional plasma. We use the massively parallel code F3D[45] to perform two-dimensional numerical simulations of resistive MHD. Equations (1)–(5) are evolved explicitly using the trapezoidal leapfrog method in time and finite difference in space. Magnetic field strengths, mass densities, velocities, lengths, times, electric fields, pressures, and resistivities are normalized to representative values of B_0, ρ_0, the Alfvén speed $c_{A0}=B_0/(4\pi\rho_0)^{1/2}$, L_0, $t_0=L_0/c_{A0}$, $E_0=c_{A0}B_0/c$, $P_0=\rho_0 c_{A0}^2$, and $\eta_0=4\pi c_{A0}L_0/c^2$, respectively.

The computational domain is of size $L_x\times L_z=409.6\times 204.8L_0$ with a cell size of $0.1\times 0.1L_0$ and uses periodic boundary conditions. The initial magnetic field profile is a double tearing mode configuration,

$$B_x(z) = \begin{cases} -B_{01}\tanh\left(\dfrac{z-L_z/4}{w_0}\right) & \dfrac{L_z}{4} < z < \dfrac{L_z}{2} \\ -B_{02}\tanh\left(\dfrac{z-L_z/4}{w_0}\right) & 0 < z < \dfrac{L_z}{4} \end{cases} \tag{36}$$

with an initial current sheet width of $w_0=2.0L_0$, and the same field reflected about $z=0$ for $-L_z/2<z<0$. Simulations are performed for $[B_{01},B_{02}]=[1,1],[1,2],[1,3],[1,4],[1,5]$, and $[2,4]$ in units of B_0. We initially have a uniform density of ρ_0 with the pressure profile uniquely determined by enforcing total global pressure balance and taking the minimum value of the plasma $\beta_{\min}=8\pi P/B_{\max}^2=1$, where $B_{\max}=\max(B_{01},B_{02})$. Therefore, the initial temperature profile is asymmetric. Reconnection is initiated using a coherent magnetic perturbation of $\mathbf{B}=-(0.012B_0L_z/2\pi)\hat{\mathbf{z}}\times\nabla[\sin(2\pi x/L_x)\sin^2(2\pi z/L_z)]$. The resistivity $\eta=0.05\eta_0$ is constant and uniform and the ratio of specific heats γ is 5/3. There is no viscosity, but fourth-order diffusion with coefficient $0.0001L_0^3 c_{A0}$ is used in all of the equations to damp noise at the grid scale. Initial random perturbations on the magnetic field of amplitude either 0.00005 or 0.0001 B_0 and on the velocity of amplitude 0.08 c_{A0} break the symmetry so that any secondary magnetic islands that form are ejected from the X-line.

The simulations are evolved until transient effects have subsided and a quasi-steady-state is achieved. The reconnected flux ψ as a function of time is shown for each of the six simulations in Fig. 3. The out-of-plane current density J_y is plotted in Fig. 4(a) for the $[B_{01},B_{02}]=[1,3]$ simulation, though this plot is representative of all of the asymmetric simulations. There is a characteristic "bulge" of the island as it grows preferentially into the weak field side, as has been reported in essentially every previous study of reconnection with asymmetric magnetic fields.

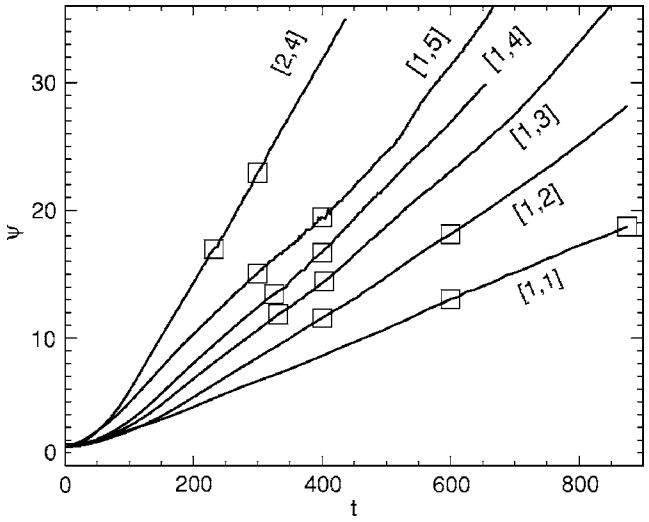

FIG. 3. Reconnected flux ψ as a function of time t for each of the simulations performed. The boxes denote the times over which steady-state quantities are averaged.

An important result of the present study is the elucidation of the decoupling of the X-line and the stagnation point. That this is the case is shown in Fig. 4(b) from the same $[1,3]$ simulation. Plotted is a cut of J_y across the X-line (scaled up by a factor of 3 to make it more visible) and the reconnecting magnetic field B_x as the dotted and (blue) solid lines, respectively. The inflow velocity v_z is plotted as the (red) dashed line using the vertical scale on the right. Care must be taken to measure v_z because the X-line is moving in the inflow direction (see the discussion in the following section). The velocity of the X-line is determined as the time rate of change of the y coordinate of the X-line, which is 0.007 for the time slice plotted. The velocity data above, therefore, have been shifted up by 0.007 in order to be in the frame of the moving X-line. Clearly, there is a nonzero velocity at the X-line, and the stagnation point occurs at a distinct point shifted toward the strong field plasma, as predicted by the theory.

Notice that the peak of J_y does not occur at the X-line, denoted by the vertical dashed line. This is interesting in light of the required balance in Ohm's law. Figure 4(c) shows the different terms in Ohm's law; the resistive contribution ηJ_y is the dotted line, the convective contribution $v_z B_x$ (in the moving frame of the X-line) is the (blue) solid line, and their sum is the dashed line. The total electric field is essentially uniform, as it must be in the steady state. Note, however, that in between the X-line and the stagnation point, the resistive term is larger than the reconnection electric field and the convection term is negative. Therefore, the resistivity actually serves to increase the magnetic field immediately to the left of the X-line, unlike in symmetric Sweet-Parker reconnection.

To perform quantitative comparisons with the theory in the preceding section, salient quantities are measured by averaging over a suitably steady time. These times are marked by boxes in Fig. 3. The reconnection electric field E is measured as ηJ_X, where J_X is the out-of-plane current density evaluated at the X-line. The outflow speed v_{out} is measured as the average of the maximum total velocity from the left and right sides of the dissipation region. The length of the dissipation region L is measured as the half-width at $1/e$ of the maximum of the out-of-plane current density J_y in a cut across the X-line in the outflow direction.

The measurements of the thicknesses δ and the magnetic field strengths B_1 and B_2 are challenging due to an extra piece of physics specific to collisional reconnection. In the numerical simulations, a purely resistive layer is observed on the strong field side, below the edge labeled *CD* in Fig. 1. In

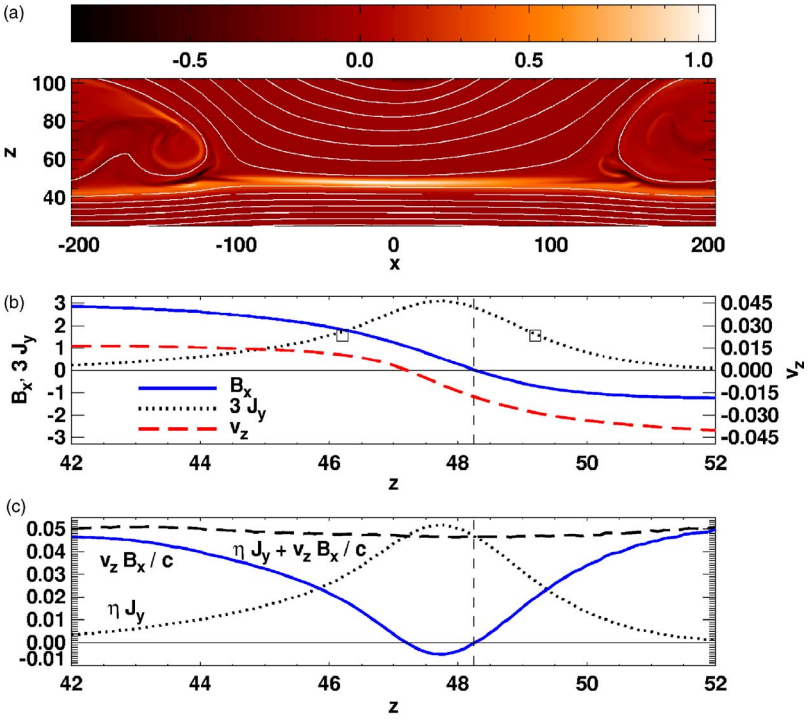

FIG. 4. (Color online) (a) The out-of-plane current density J_y (grayscale) and the magnetic field lines (the contours) for the $[B_{01},B_{02}]=[1,3]$ simulation. The aspect ratio of the plot is not to scale. (b) A cut across the X-line in the inflow (z) direction of the reconnecting magnetic field B_x (solid line, blue), the out-of-plane current density J_y (dotted line), and the inflow speed v_z in the frame of the moving X-line (dashed line, red). We have scaled J_y by a factor of 3 to make it more visible. The vertical dashed line marks the X-line. The peak in J_y does not occur at the X-line and v_z does not go through zero at the X-line. (c) The terms in Ohm's law for the same simulation, namely the convection term in the frame of the moving X-line (solid line, blue), the resistive term (dotted line), and their sum (dashed line).

this diffusive layer, there is no outflow and the inflow velocity does not change, but the magnetic field diffuses, leaving the field at the edge of the dissipation region (the salient field for determining the outflow speed) smaller than its asymptotic value B_{02}. In other words, the outflow jet is narrower than the out-of-plane current on the strong field side. As such, the method often used to measure the thickness, the half-width at half-maximum of the out-of-plane current density, overestimates the value. Therefore, care must be taken to eliminate the effect of the purely resistive part of the current sheet in making these measurements.

In light of the above discussion, we measure the thicknesses δ_{X1} and δ_{X2} by finding the maximum in the out-of-plane current density J_y in a cut across the X-line. [Note, the maximum of J_y does not occur at the X-line; see Fig. 4(b)]. Then, δ_{X1} (the value on the weak field side) is defined as the distance from the half-maximum of J_y to the X-line. See the box to the right of the X-line in Fig. 4(b). To eliminate the purely diffusive part of the current on the strong field side, we assume that the current is symmetric about its maximum, and find where the half-maximum would be. Then, δ_{X2} is the distance from that point to the X-line. See the box to the left of the X-line in Fig. 4(b). The effect is not a large one for the smaller field simulations, but becomes more important for the $[B_{01},B_{02}]=[1,4]$ and [1,5] simulations. The quantity δ_{XS} is measured directly as the distance between the X-line and the point on the strong field side where J_y goes through the same value as it does at the X-line. Equations (20) and (21) are used to calculate δ_{S1} and δ_{S2}.

The upstream magnetic field strengths B_1 and B_2 are measured by taking a cut in the z direction of the outflow velocity a distance of $(3/4)L$ downstream of the X-line, finding where the outflow has fallen off to $1/e^2 \sim 0.13$ of its peak value both above and below the neutral line, mapping these distances back to the X-line, and measuring the magnetic field strength at this distance above and below the X-line. This method ensures that the measured value is representative of the field driving the outflow. The reason we go only 3/4 of the way down the sheet to make this measurement is that the opening out of the sheet into the island skews the measurement if taken too far down the sheet. If instead of the present method we measure the upstream field by finding the field where the symmetrized out-of-plane current goes through $1/e^2$ of its maximum, the results are not very different. The time-averaged inflow velocities in the frame of the moving X-line are calculated indirectly as the predicted reconnection rate E divided by the appropriate upstream field B_1 or B_2.

The measured quantities are given as the first eight rows in Table I. The uncertainties of the measured quantities are estimated as the standard deviation of the time average. The uncertainties for E, v_{out}, L, B, and δ are approximately 5%, 4%, 7%, 6%, and 7%, respectively.

To check the theory in Sec. II, we test the veracity of the conservation laws for energy and mass. The plots in Fig. 5 show the energy conservation (a) through the whole dissipation region [the box *ABCD* in Fig. 1 as described by Eq. (11)], (b) above the neutral line [*ABXW* as described by Eq. (22)], and (c) below the neutral line [*CDXW* as described by Eq. (23)] and the mass conservation, (d) through the whole dissipation region [*ABCD* as described by Eq. (10)], (e) above the line through the stagnation point [*ABST* as described by Eq. (24)], and (f) below the line through the stagnation point [*CDST* as described by Eq. (25)]. For each plot, the influx is plotted on the horizontal axis, the outflux is on the vertical axis, and the dashed line with a slope of 1 marks their predicted equality. The agreement is within the stated uncertainties, which is about 10% for each of these plots, using standard propagation of error techniques. The plot in (f) shows the data are bunched around a similar value for many of the simulations; this is because the v_2 dependence on B_2 is rather weak and as B_{02} increases, the size of the purely diffusive layer increases, leading to a less dramatic change in B_2 for a given change in B_{02}.

TABLE I. Measured and calculated quantities from the numerical simulations. The first eight rows are quantities measured directly from the simulation output. (See the text for how they are obtained and normalized.) The final five rows use Eqs. (32), (33), (30), (15), and (35), respectively, using values from the first three rows to calculate the predictions, for the quantities in rows 4–8.

B_{01},B_{02}	[1,1]	[1,2]	[1,3]	[1,4]	[1,5]	[2,4]
B_1	0.90	1.03	1.02	1.06	0.95	2.08
B_2	0.88	1.70	2.38	2.82	3.22	3.35
L	86	94	111	107	112	106
δ_{X1}	2.15	1.56	1.35	1.20	1.08	1.20
δ_{X2}	2.15	2.45	2.71	2.89	3.09	1.93
δ_{XS}	0.01	0.84	1.40	1.60	1.94	0.67
v_{out}	0.93	1.33	1.61	1.80	1.86	2.54
E	0.023	0.035	0.041	0.047	0.046	0.092
δ_{X1}	2.21	1.47	1.23	1.08	0.97	1.11
δ_{X2}	2.18	2.42	2.88	2.86	3.29	1.80
δ_{XS}	0.00	0.95	1.65	1.78	2.33	0.68
v_{out}	0.89	1.32	1.56	1.73	1.75	2.63
E	0.020	0.035	0.041	0.049	0.048	0.093

The predictions relating upstream magnetic fields and densities to the reconnection parameters δ_{X1}, δ_{X2}, δ_{XS}, v_{out}, and E are tested using Eqs. (32), (33), (30), (15), and (35). The numerical results are shown in the final five rows of Table I to compare with the raw data in rows 4–8.

The scaling is more easily seen in the plots. Figure 6 shows (a) the predicted and measured outflow speeds using Eq. (15) for symmetric densities, (b) the reconnection rate E in terms of the geometry as predicted in Eq. (19), and (c) the reconnection rate E purely in terms of upstream quantities as predicted in Eq. (35). Propagation of error for the quantities on the horizontal axes in Figs. 6(a)–6(c) gives uncertainties of 4%, 15%, and 6%, respectively. The agreement between theory and simulation for these plots is very good within the stated uncertainties.

Plots (a) and (b) of Fig. 7 show the measured and predicted values of the thicknesses δ_{X1} and δ_{X2} in terms of upstream quantities as given in Eqs. (32) and (33). Plot (c) shows the scaling of δ_{X2}/δ_{X1} and δ_{S1}/δ_{S2} versus B_2/B_1 as dots and diamonds, respectively, which tests Eqs. (26) and (27). The agreement in the δ plots is again quite good, within

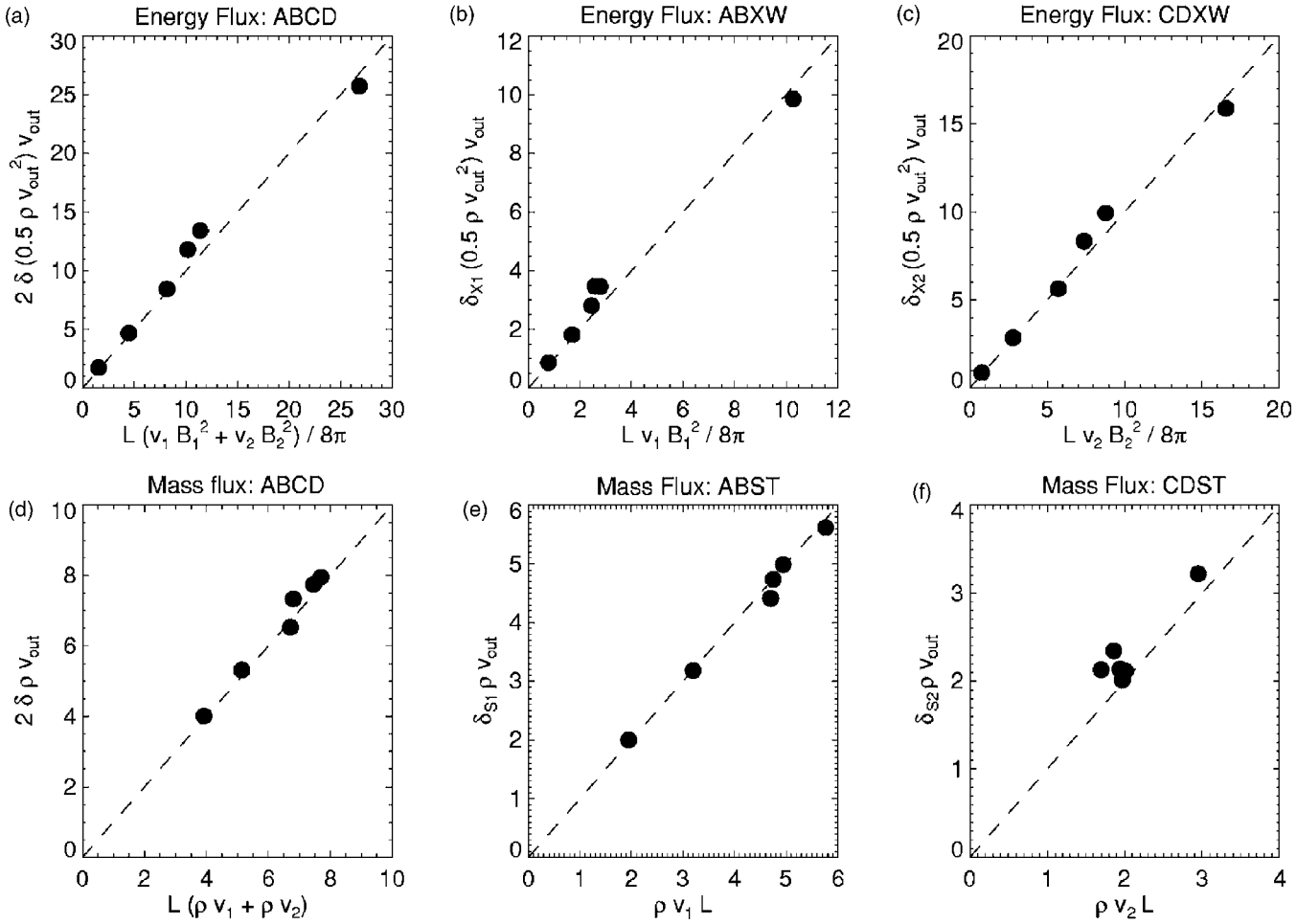

FIG. 5. Verification of conservation of energy and mass flux through various subregions of the dissipation region defined in Fig. 1. Plotted are energy flux through (a) the whole dissipation region *ABCD*, (b) the region above the X-line *ABXW*, (c) the region below the X-line *CDXW*, and the mass flux (d) through the whole region *ABCD*, (e) the region above the stagnation point *ABST*, and (f) the region below the stagnation point *CDST*. Influx is on the horizontal axis, outflux is on the vertical axis, and the dashed lines are the predicted slope of 1 from Eqs. (10), (11), and (22)–(25).

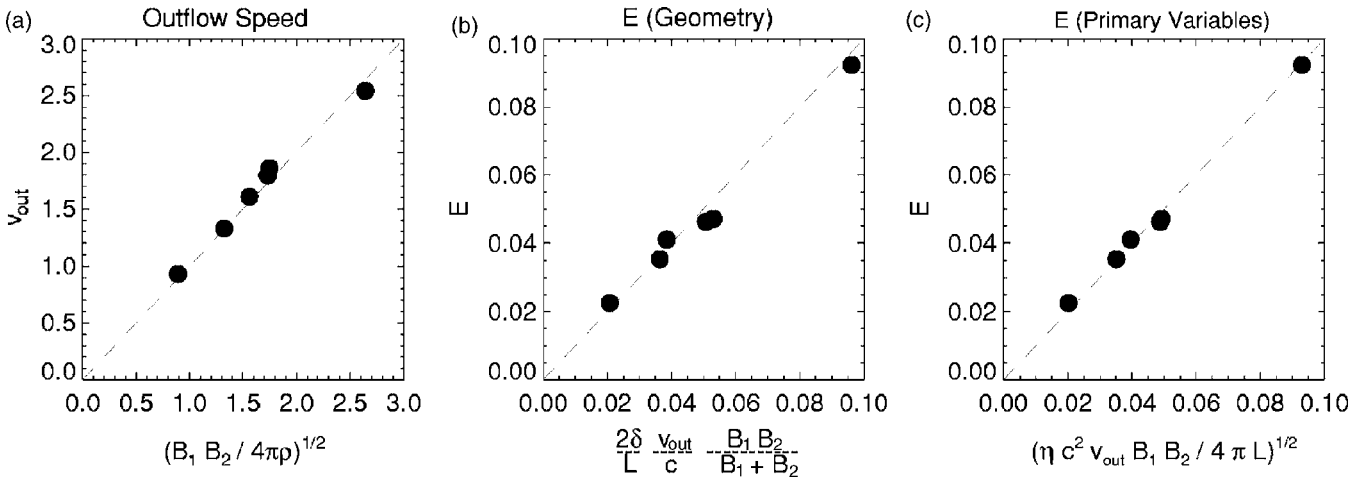

FIG. 6. (a) Measured and calculated values of the outflow velocity v_{out} using Eq. (15). Measured and calculated values of the reconnection rate E, using the general expression relating E to (b) the geometry of the dissipation region, as given by Eq. (19), and (c) to the upstream densities and magnetic fields as given by Eq. (35). The dashed line has the predicted slope of 1.

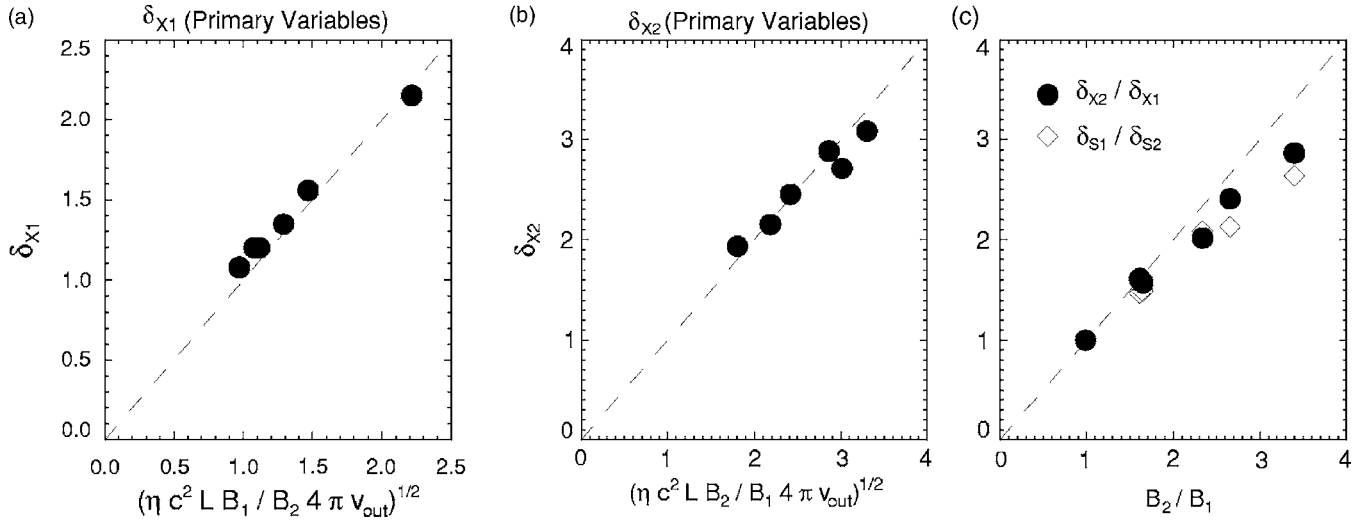

FIG. 7. Measured and calculated values of (a) δ_{X1} and (b) δ_{X2} from the predictions of Eqs. (32) and (33). (c) Plot of δ_{X2}/δ_{X1} (dots) and δ_{S1}/δ_{S2} (diamonds) as a function of B_2/B_1. The dashed line has the predicted slope of 1 from Eqs. (26) and (27).

the 12% uncertainty found using propagation of errors. The data in Fig. 7(c) compare fairly well to the estimated uncertainty of 10%, but show some effects of the purely diffusive layer outside of the dissipation region for larger B_{02}.

A look at the raw data confirms the predictions of Eq. (29), which, in the limit of uniform density, predicts $\delta_{S1}=\delta_{X1}+\delta_{XS}\sim\delta_{X2}$ and $\delta_{S2}=\delta_{X2}-\delta_{XS}\sim\delta_{X1}$. In other words, the dissipation region is symmetric around the peak in the out-of-plane current, modulo the purely diffusive region. As such, Eq. (30) is automatically satisfied, as well.

The present simulations were performed with asymmetric fields but symmetric densities. A recent study[40] considered the complementary case of asymmetric densities with symmetric fields. Their study used an anomalous localized resistivity. They found that the reconnection rate was proportional to an Alfvén speed based on an average of their densities, in agreement with Eqs. (14) and (19). Furthermore, their outflow jets were displaced toward the low-density plasma, in qualitative agreement with Eq. (27).

IV. OBSERVATIONAL SIGNATURES

In this section, we highlight general observational signatures of asymmetric reconnection. These signatures are discussed for particular systems in Sec. V. We have already noted the "bulge" due to the island growing preferentially into the weak field side, which occurs because it is easier for the newly reconnected field lines to bend the weaker field than the stronger field upstream of the island.

We also observe that the X-line itself drifts in the *inflow* direction toward the plasma with the stronger magnetic field, in the reference frame of the simulation. This effect is often not observed in simulations because of the use of a stationary localized resistivity. It was first observed in simulations by Ugai,[23] and is also apparent in the results of Refs. 24 and 31, none of which used fixed anomalous resistivity. The physical cause of the drift is relatively simple. In symmetric reconnection, magnetic field lines upstream of the dissipation region bend due to the opposing influences of the inflow at the dissipation region and the island expanding downstream. When the magnetic fields are asymmetric, it takes more energy to bend the magnetic fields on the strong field side than it takes for the X-line to propagate toward the strong field. As such, the drift speed of the X-line can be comparable to the inflow speed on the strong field side. For the present simulations, $v_2\sim cE/B_2=0.041/2.38=0.017$ for the data shown in Figs. 4(b) and 4(c), while the drift speed is 0.007. This is consistent with the physical picture presented here, as first stated by Ugai.[23]

We have already noted that the X-line and stagnation point are not colocated in asymmetric reconnection. This fact has important observational consequences. In particular, the location of the stagnation point relative to the X-line determines which plasma crosses the X-line and, therefore, on which side of the X-line the mixing of the plasmas will occur. We find that the stagnation point will be on whichever side of the X-line has the higher Alfvén speed. To derive this, note that the stagnation point is on the strong field side of the X-line if $\delta_{X2}>\delta_{S2}$. Using Eqs. (28) and (17), this expression is equivalent to

$$c_{A2}>c_{A1}, \tag{37}$$

where $c_{Ai}=B_i/(4\pi\rho_i)^{1/2}$ for $i=1,2$. Similarly, if $c_{A1}>c_{A2}$, the stagnation point is shifted toward the weak field plasma of the X-line. Therefore, whichever plasma has the smaller Alfvén speed will flow across the X-line. We discuss applications of this result to the magnetosphere in the next section.

Another interesting signature is the profile of the reconnecting magnetic field in a cut across the X-line. In symmetric Sweet-Parker reconnection, the profile is well fit by a tanh profile. For asymmetric reconnection, the simulation results suggest that the profile is well fit by a piecewise tanh function as opposed to a shifted tanh function of the form $B_x(z)=B_{\text{avg}}+B_{\text{diff}}[\tanh(z/w_0)]$. To ensure that this profile is not a consequence of the initial conditions that used a piecewise tanh profile, we perform a simulation with initial conditions

TABLE II. Summary of the key results for observations of asymmetric reconnection. The subscripts "1," "2," and "out" refer to upstream values on either side of the dissipation region and values for the outflow. The stagnation point lies on whichever side of the X-line has the larger Alfvén speed.

Physical quantity	Result
Density of outflow, Eq. (17)	$\rho_{out} \sim (\rho_1 B_2 + \rho_2 B_1)/(B_1+B_2)$
Outflow speed, Eq. (13)	$v_{out}^2 \sim [(B_1 B_2)/(4\pi)][(B_1+B_2)/(\rho_1 B_2+\rho_2 B_1)]$
Reconnection rate, Eq. (19)	$E \sim [(B_1 B_2)/(B_1+B_2)](v_{out}/c)(2\delta/L)$
Location of X-line, Eq. (26)	$(\delta_{X2}/\delta_{X1}) \sim (B_2/B_1)$
Location of stagnation point, Eq. (27)	$(\delta_{S2}/\delta_{S1}) \sim (\rho_2 B_1/\rho_1 B_2)$

of a shifted tanh. We find that even with these initial conditions, the steady-state configuration is best fit by a piecewise tanh function.

Finally, as noted in the preceding section, the resistive simulations performed here displayed a purely diffusive layer outside of the layer formed by the outflow jet on the strong field side, which can be seen in Fig. 4(b). This layer may be expected to be present, for example, in laboratory experiments of collisional plasmas. However, the present simulations were done with an exceptionally large resistivity, so the layer is unlikely to be prevalent in laboratory plasmas at ambient resistivities. It is not expected to exist at all in collisionless asymmetric reconnection.

V. DISCUSSION

In this paper, we have generalized the Sweet-Parker model of resistive reconnection to allow for upstream plasmas with different magnetic field strengths and densities. In particular, we have derived scaling laws from first principles for the reconnection rate, outflow speed, and structure of the dissipation region in terms of the upstream densities and fields. A summary of the predictions potentially useful to observations is collected in Table II. These results are derived without appealing to a particular dissipation mechanism, and therefore are generally valid.

We have verified the theory in the limit of asymmetric magnetic field with symmetric density using numerical simulations of resistive MHD. The theory is also in good agreement with recent MHD with anomalous resistivity simulations of reconnection with asymmetric density and symmetric fields.[40]

The analysis has elucidated the decoupling of the X-line from the stagnation point during asymmetric reconnection. The position of the X-line within the dissipation region is set by the balance of energy flux, while the position of the stagnation point is set by the balance of mass flux. For arbitrary upstream parameters, these two points need not be coincident. This is a generic feature of asymmetric reconnection.

Observational signatures of asymmetric reconnection were also discussed. We find that in addition to the well-studied bulge due to the island growing preferentially into the weak field plasma, the dissipation region drifts into the strong field plasma, as first observed in Ref. 23. Further, we have shown that the X-line is closer to the weak field plasma than the strong field plasma, and the stagnation point is on whichever side of the X-line that the Alfvén speed is larger. As such, plasma from the side with the smaller Alfvén speed flows across the X-line.

The most obvious potential application of the present result is for asymmetric reconnection in the magnetosphere, specifically at the dayside magnetopause. Typical parameters are $B_{sh} \sim 20$ nT, $n_{sh} \sim 20$ cm^{-3}, $B_{sp} \sim 50$ nT, and $n_{sp} \sim 0.5$ cm^{-3},[7,8] where the "sh" subscript refers to the magnetosheath and "sp" refers to the magnetosphere. As such, the bulge extends into the magnetosheath, as has been reported often in observations. Further, since $c_{A,sh} < c_{A,sp}$, the stagnation point is on the magnetosphere side of the X-line. Therefore, there is a flow of magnetosheath plasma across the X-line into the magnetosphere. This is in agreement with the numerical results of Ref. 46, as well as many of the numerical studies in the Introduction and many satellite observations. The values for the outflow speed and the reconnection electric field using the typical parameters quoted earlier are $v_{out} \sim 180$ km/s and $E \sim 0.52$ mV/m, respectively, assuming a dissipation region aspect ratio δ/L of 0.1.

Another application is in asymmetric reconnection in the magnetotail, as in the Øieroset *et al.* study using Wind observations.[14] In particular, they measured parameters of $B_1 = 8.8$ nT, $n_1 = 0.1$ cm^{-3}, $B_2 = 10.3$ nT, and $n_2 = 0.01$ cm^{-3}. While a naive average of the two densities would give 0.055 cm^{-3}, the prediction for the density in the outflow region using Eq. (17) is $n_{out} = 0.059$ cm^{-3}, in excellent agreement with the measured value of $n_{out} = 0.06$ cm^{-3}. Future comparative studies of asymmetric reconnection in the magnetopause and magnetotail would be very interesting.

The results presented here comprise only part of a more general understanding of reconnection in realistic physical systems. The present results still assume antiparallel magnetic fields. In the uniform density case, the introduction of a uniform out-of-plane (guide) field should not affect the results.[23] However, if there is a density gradient across the dissipation region, the reconnection will be qualitatively different in the presence of a guide field because of the introduction of diamagnetic drifts in the outflow direction, which has been shown to reduce the reconnection rate.[39,47]

The addition of an asymmetric guide field (i.e., a system with field lines of arbitrary strength at arbitrary angles) is also an interesting problem. It is not even clear in which plane the reconnection will predominantly occur.[34] It has been conjectured[41] that in such a system, the plane of recon-

nection will be determined by maximizing the outflow speed given by Eq. (13).

Future studies should also consider asymmetric Hall reconnection, which is orders of magnitude faster than Sweet-Parker reconnection[5,6] and is imperative for applications in the magnetosphere and laboratory plasmas. In antiparallel symmetric Hall reconnection, the thicknesses of the ion and electron dissipation regions are of order of the ion and electron skin depths c/ω_{pi} and c/ω_{pe}. These length scales depend on the density. A subject of much debate is the dependence of the Hall reconnection process on the ion skin depth c/ω_{pi}. If the Hall reconnection rate is independent of c/ω_{pi}, with the length of the dissipation region $\sim 10c/\omega_{pi}$, as argued in Refs. 45 and 48–50, then what is the aspect ratio of the dissipation region (which impacts the reconnection rate) when the reconnecting plasmas have different skin depths? Alternately, if the reconnection rate depends on c/ω_{pi}, as argued in Refs. 51–55, how will the reconnection rate scale for a system with different skin depths? More importantly, a study of asymmetric Hall reconnection may elucidate which of the scenarios is, in fact, correct.

Limitations of the fluid simulations performed here include using a constant and uniform resistivity instead of a Spitzer resistivity related to the temperature and not including Joule heating.

ACKNOWLEDGMENTS

The authors would like to thank Joachim Birn, Joe Borovsky, and Michael Hesse for interesting conversations.

This work was supported by NASA Grant No. NNG05GM98G and NSF Grant No. ATM-0645271. Computations were carried out at the National Energy Research Scientific Computing Center.

[1] P. A. Sweet, in *Electromagnetic Phenomena in Cosmical Physics*, edited by B. Lehnert (Cambridge University Press, New York, 1958), p. 123.
[2] E. N. Parker, J. Geophys. Res. **62**, 509 (1957).
[3] H. E. Petschek, in *AAS/NASA Symposium on the Physics of Solar Flares*, edited by W. N. Ness (NASA, Washington, D.C., 1964), p. 425.
[4] D. Biskamp, *Magnetic Reconnection in Plasmas* (Cambridge University Press, Cambridge, 2000), p. 199.
[5] J. Birn, J. F. Drake, M. A. Shay, B. N. Rogers, R. E. Denton, M. Hesse, M. Kuznetsova, Z. W. Ma, A. Bhattacharjee, A. Otto, and P. L. Pritchett, J. Geophys. Res. **106**, 3715, DOI: 10.1029/1999JA900449 (2001).
[6] J. F. Drake and M. A. Shay, in *Reconnection of Magnetic Fields*, edited by J. Birn and E. R. Priest (Cambridge University Press, Cambridge, 2007), p. 87.
[7] T. D. Phan and G. Paschmann, J. Geophys. Res. **101**, 7801, DOI: 10.1029/95JA03752 (1996).
[8] H. C. Ku and D. G. Sibeck, J. Geophys. Res. **102**, 2243, DOI: 10.1029/96JA03162 (1997).
[9] C. T. Russell and R. C. Elphic, Space Sci. Rev. **22**, 681 (1978).
[10] C. T. Russell and R. C. Elphic, Geophys. Res. Lett. **6**, 33 (1979).
[11] J. Sanny, C. Beck, and D. G. Sibeck, J. Geophys. Res. **103**, 4683, DOI: 10.1029/97JA03246 (1998).
[12] J. E. Borovsky and J. T. Steinberg, J. Geophys. Res. **111**, A07S10, DOI: 10.1029/2005JA011397 (2006).
[13] J. E. Borovsky and M. H. Denton, Geophys. Res. Lett. **33**, L20101, DOI: 10.1029/2006GL026519 (2006).
[14] M. Øieroset, T. D. Phan, and M. Fujimoto, Geophys. Res. Lett. **31**, L12801, DOI: 10.1029/2004GL019958 (2004).
[15] J. T. Gosling, M. F. Thomsen, S. J. Bame, R. C. Elphic, and C. T. Russell, J. Geophys. Res. **95**, 8073 (1990).
[16] J. T. Gosling, S. Eriksson, R. M. Skoug, D. J. McComas, and R. J. Forsyth, Astrophys. J. **644**, 613 (2006).
[17] R. H. Levy, H. E. Petschek, and G. L. Siscoe, AIAA J. **2**, 2065 (1964).
[18] M. Hoshino and A. Nishida, J. Geophys. Res. **88**, 6926 (1983).
[19] M. Scholer, J. Geophys. Res. **94**, 15099 (1989).
[20] Y. Shi and L. C. Lee, Planet. Space Sci. **38**, 437 (1990).
[21] Y. Lin and L. C. Lee, Space Sci. Rev. **65**, 59 (1993).
[22] A. L. L. Belle-Hamer, A. Otto, and L. C. Lee, J. Geophys. Res. **100**, 11875, DOI: 10.1029/95JA00969 (1995).
[23] M. Ugai, Phys. Plasmas **7**, 867 (2000).
[24] S. P. Jin, J. T. Shen, L. Hao, and X. P. Hu, Sci. China, Ser. E: Technol. Sci. **43**, 129 (2000).
[25] E. Lee, K. W. Min, D. Y. Lee, J. Seon, and K. J. Hwang, Phys. Plasmas **9**, 5070 (2002).
[26] Y. Lin and H. Xie, Geophys. Res. Lett. **24**, 3145, DOI: 10.1029/97GL03278 (1997).
[27] N. Omidi, H. Karimabadi, and D. Krauss-Varban, Geophys. Res. Lett. **25**, 3273, DOI: 10.1029/98GL02484 (1998).
[28] D. Krauss-Varban, H. Karimabadi, and N. Omidi, Geophys. Res. Lett. **26**, 1235, DOI: 10.1029/1999GL900211 (1999).
[29] M. Nakamura and M. Scholer, J. Geophys. Res. **105**, 23179, DOI: 10.1029/2000JA900101 (2000).
[30] H. Xie and Y. Lin, J. Geophys. Res. **105**, 25171, DOI: 10.1029/2000JA000143 (2000).
[31] Y. Lin, J. Geophys. Res. **106**, 25451, DOI: 10.1029/2000JA000184 (2001).
[32] H. Okuda, J. Geophys. Res. **98**, 3953 (1993).
[33] H. E. Petschek and R. M. Thorne, Astrophys. J. **147**, 1157 (1967).
[34] B. U. O. Sonnerup, J. Geophys. Res. **79**, 1546 (1974).
[35] S. W. H. Cowley, J. Plasma Phys. **12**, 341 (1974).
[36] V. S. Semenov, I. V. Kubyshkin, M. F. Heyn, and H. K. Biernat, J. Plasma Phys. **30**, 321 (1983).
[37] M. F. Heyn, H. K. Biernat, R. P. Rijnbeek, and V. S. Semenov, J. Plasma Phys. **40**, 235 (1988).
[38] H. Karimabadi, D. Krauss-Varban, N. Omidi, and H. X. Vu, J. Geophys. Res. **104**, 12313, DOI: 10.1029/1999JA900089 (1999).
[39] M. Swisdak, J. F. Drake, M. A. Shay, and B. N. Rogers, J. Geophys. Res. **108**, 1218, DOI: 10.1029/2002JA009726 (2003).
[40] J. E. Borovsky and M. Hesse, Phys. Plasmas **14**, 102309 (2007).
[41] M. Swisdak and J. F. Drake, Geophys. Res. Lett. **34**, L11106, DOI: 10.1029/2007GL029815 (2007).
[42] D. Biskamp, Phys. Fluids **29**, 1520 (1986).
[43] D. A. Uzdensky and R. M. Kulsrud, Phys. Plasmas **7**, 4018 (2000).
[44] B. D. Jemella, J. F. Drake, and M. A. Shay, Phys. Plasmas **11**, 5668 (2004).
[45] M. A. Shay, J. F. Drake, M. Swisdak, and B. N. Rogers, Phys. Plasmas **11**, 2199 (2004).
[46] J. C. Dorelli, M. Hesse, M. M. Kuznetsova, L. Rastaetter, and J. Raeder, J. Geophys. Res. **109**, A12216, DOI: 10.1029/2004JA010458 (2004).
[47] K. Germaschewski, A. Bhattacharjee, C. S. Ng, X. Wang, and L. Chacon, Bull. Am. Phys. Soc. **51**, 312 (2006).
[48] M. A. Shay, J. F. Drake, B. N. Rogers, and R. E. Denton, Geophys. Res. Lett. **26**, 2163, DOI: 10.1029/1999GL900481 (1999).
[49] J. D. Huba and L. I. Rudakov, Phys. Rev. Lett. **93**, 175003 (2004).
[50] P. A. Cassak, J. F. Drake, M. A. Shay, and B. Eckhardt, Phys. Rev. Lett. **98**, 215001 (2007).
[51] D. Grasso, F. Pegoraro, F. Porcelli, and F. Califano, Plasma Phys. Controlled Fusion **41**, 1497 (1999).
[52] X. Wang, A. Bhattacharjee, and Z. W. Ma, Phys. Rev. Lett. **87**, 265003 (2001).
[53] F. Porcelli, D. Borgogno, F. Califano, D. Grasso, M. Ottaviani, and F. Pegoraro, Plasma Phys. Controlled Fusion **44**, B389 (2002).
[54] R. Fitzpatrick, Phys. Plasmas **11**, 937 (2004).
[55] A. Bhattacharjee, K. Germaschewski, and C. S. Ng, Phys. Plasmas **12**, 042305 (2005).